Original

Sharifi, P.; Eckerlebe, H.; Marlow, F.:

SANS analysis of opal structures made by the capillary deposition method

In: Physical Chemistry Chemical Physics (2012) RSC Publishing

DOI: 10.1039/c2cp40825b

PCCP

Cite this: *Phys. Chem. Chem. Phys.*, 2012, **14**, 10324–10331

www.rsc.org/pccp

PAPER

SANS analysis of opal structures made by the capillary deposition method

P. Sharifi,[a] H. Eckerlebe[b] and F. Marlow*[ac]

Received 15th March 2012, Accepted 18th May 2012
DOI: 10.1039/c2cp40825b

Small angle neutron scattering (SANS) is used to analyze the structure of opals and inverse opals made by the capillary deposition method. We show that there is no deformation in special lattice directions such as the growth direction and the support plane direction. However, effects of twinning of the dense-packed structure and plane-like lattice perturbations have been observed. The latter appear as linear surface disturbances. We propose a model with an anisotropic distribution of stacking faults which delivers the different peak intensities in the neutron diffraction pattern. The rocking curves show that small perfect crystal parts are aligned better than $\pm 3^\circ$ and $\pm 11^\circ$ for the opals and inverse opals, respectively.

1 Introduction

Photonic crystals are periodic dielectric structures. They can manipulate the propagation and emission of light.[1,2] Many methods have been used for their fabrication. Among them the self-assembly of colloidal particles is a low-cost and simple method which forms so-called artificial opals.

Different self-assembly methods such as the vertical deposition (VD)[3] and the capillary deposition method (CDM)[4] deliver a close-packed structure with face-centered cubic (fcc) symmetry. Even though this structure is common for different fabrication methods, specific differences are expected with respect to their detailed configuration of lattice perturbations including stacking faults, mosaic structures, and twinning.[5]

Among the characterization methods, neutron and X-ray scattering offer comprehensive information on the lattice ordering. In recent years, only a few groups have intensively dealt with this problem.[6–10] They focused on direct and inverse opals made by the VD method and on natural opals (see also ref. 11). The reconstruction of the reciprocal space[8] and the proposal of stacking fault models[9] are two examples of these efforts.

Even though the VD method and CDM belong to the same class of opal deposition method with respect to the assembly deriving force,[5] they are different in important aspects. Deposition and drying are separated in CDM in contrast to vertical deposition, where these two steps occur simultaneously. This difference can be used to assign the influence of specific fabrication steps to properties of the formed lattice.[12] This may help in gaining a better understanding of the self-assembly mechanism.

In this paper we report on SANS measurements on direct and inverse opal films made by the CDM. The data are analyzed with respect to inherent lattice disturbances, post-synthesis deformations, stacking fault arrangements, and mosaic structure of the films. The shrinkage process in opal drying does not induce preferred orientational effects in the lattice. The observed asymmetries in diffraction peak intensities can be explained by a non-symmetric stacking fault distribution. The measured rocking curves are explained by the mosaic spread of the opal lattice.

2 Experimental section

Materials

A suspension of 0.5 wt% polystyrene (PS) spheres with a diameter of (0.264 ± 0.008) μm was prepared by dilution of the 5 wt% commercial product (Microparticles GmbH) with de-ionized water.

Glass slides (Menzel-Gläser) used as supports were cleaned in two steps. First, they were immersed in an aqueous solution of 5% Labosol (Neolab) for 30 minutes. After rinsing with water, they were immersed in 0.5 M NaOH in ethanol/water (1 : 3 v/v) for 30 minutes. Finally, they were rinsed with water and dried in a flow of nitrogen.

Titanium(IV) isopropoxide (97%, alcoholic solution, Sigma-Aldrich) was diluted with ethanol (purity ≥ 99.9%, Merck) to make a 40 vol% alkoxide solution for titania inverse opal fabrication.

Opal deposition

The construction of the capillary cell and the opal deposition process as schematically shown in Fig. 1(a) are described

[a] *Max-Planck-Institut für Kohlenforschung, Kaiser-Wilhelm-Platz 1, 45470 Mülheim an der Ruhr, Germany. E-mail: marlow@mpi-muelheim.mpg.de*
[b] *GKSS, Helmholtz-Zentrum Geesthacht, Max-Planck-Straße 1, 21502 Geesthacht, Germany*
[c] *Center for Nanointegration Duisburg-Essen (CeNIDE), University of Duisburg-Essen, 47057 Duisburg, Germany*

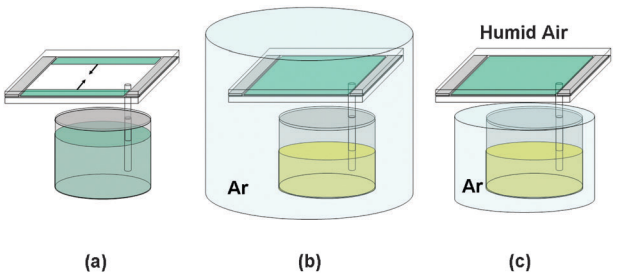

Fig. 1 Set-up for sample preparation. (a) Opal fabrication with the CDM. (b) Alkoxide infiltration under argon, and (c) alkoxide infiltration with partial argon protection. A capillary transports either a suspension (green) or a precursor solution (yellow) into a planar capillary cell or into the opal sample (darker green), respectively. The growth of the opal in (a) as well as the titania formation in (c) proceeds from the outer edge to the center of the cells.

in ref. 4 and 13. In the current work, two polymer spacers (15 μm thick) were used to ensure that film thickness is uniform across the whole cell. Capillary tubes of 1 mm external diameter and 20 mm length were used for suspension flow. The deposition was done under humidity and temperature control similar to ref. 13 (22 °C, 40% RH). The same or identically made samples have also been used in ref. 14.

Inverse opal preparation

The inversion process consisted of several steps: first, the capillary tube from opal deposition was replaced with a new one. Then, the opal film was contacted with the alkoxide solution *via* the capillary tube. The whole set-up was protected against air with an argon flow (Fig. 1(b)). After two days, the cell was exposed to air while the alkoxide solution was still protected with an argon flow (Fig. 1(c)). After about 10 days, the sample was detached from the solution and stored in air for one week. Finally, the film was heated for the removal of the polystyrene template according to the following program: 30 min from room temperature to 80 °C, 1 h at 80 °C, 1.5 h from 80 °C to 200 °C, 1 h at 200 °C, 3 h from 200 °C to 500 °C, 3 h at 500 °C and then autonomous cooling to room temperature (initial rate: -2.5 K s^{-1}).

Characterization

Scanning electron microscopy (SEM) images were taken with a Hitachi S-3500N microscope after opening the cell (separation of the two supporting glass slides) and sputtering of a 10 nm Au layer on top of the films. Confocal microscopy images were taken with an Olympus-FV300IX71 confocal microscope. The opening operation of the cell sometimes induces visible disturbances of the lattice. Since also non-obvious changes by this operation are not excluded, one has to be careful in the interpretation of the results.

A fully destruction-free characterization method for the CDM-made opal films is SANS. Especially extinction problems of the glass supports as expected for SAXS are minimal. The SANS measurements were carried out at the SANS-2 beam line of the research reactor in Geesthacht (Germany). The neutron wavelength was set to $\lambda = 0.58$ nm for this experiment (with $\Delta\lambda/\lambda = 0.1$). The sample was placed at a distance of 50 mm from the output diaphragm of SANS-2 and had a

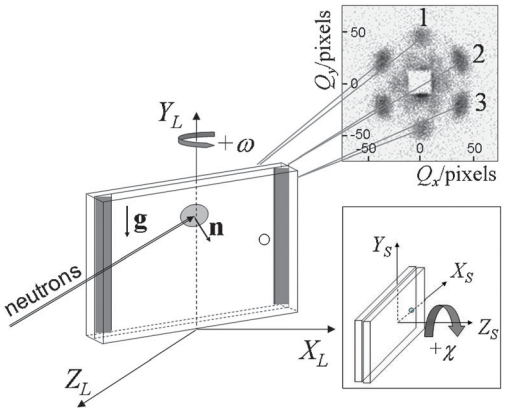

Fig. 2 The SANS sample configuration. Laboratory and sample coordinate systems are indicated with L and S indices, respectively. The Y_S axis is parallel to the growth direction and the Z_S axis is perpendicular to the sample surface. The χ-rotation turns the sample and sample system around the Z_S axis.

circular illuminated area with a diameter of about 4 mm. The scattered neutrons were detected by a position-sensitive detector with a resolution of 256 × 256 pixels; each of 2.2 × 2.2 mm^2 size. The detector–sample distance was 21.5 m. All spot positions are described in terms of pixels in this work. The (0,0) position is the beam center. The scattering vector **Q** in normal units can be calculated by the relation 1 pixel = 11.1 × 10^{-4} nm^{-1}.

The samples were mounted on a holder with two rotation axes (Fig. 2). One rotation axis was in the sample plane perpendicular to the neuron beam (ω-scan) and the other one perpendicular to the sample plane (χ-scan). The holder set-up allowed an ω-rotation of the sample in an angular range from about $-70°$ to 70° without shadowing the beam.

Typically, the measurements were carried out with irradiation times of 10 and 40 minutes for opal and inverse opal films, respectively. In two special cases, the irradiation times were increased to some hours in order to get high-resolution diffraction patterns. All intensity values I discussed in this work refer to a circle with 27 pixels in diameter which can cover a typical diffraction spot completely. If the background was subtracted from the intensity, we use the symbol I^{bs} instead of I. Normally, an averaged background is used in order to avoid the influence of background fluctuations.

3 Results and discussion

3.1 SEM and confocal microscopy

Fig. 3 shows microscopic images of opal and inverse opal films. The surface of the samples exhibits hexagonal ordering. This means that the [111] direction is parallel to the Z_S axis. The growth direction of the films is the Y_S direction which turns out to be the [1$\bar{1}$0] direction in the lattice.[13] Therefore, the X_S axis points into the [$\bar{1}\bar{1}$2] direction.

Apart from point defects sometimes visible at the surface, sets of lines appear at the surface of the opal film. They are often parallel to each other, and sometimes a symmetrical arrangement with respect to the growth direction becomes visible which is reminiscent of a fishbone type structure (Fig. 3(c)).

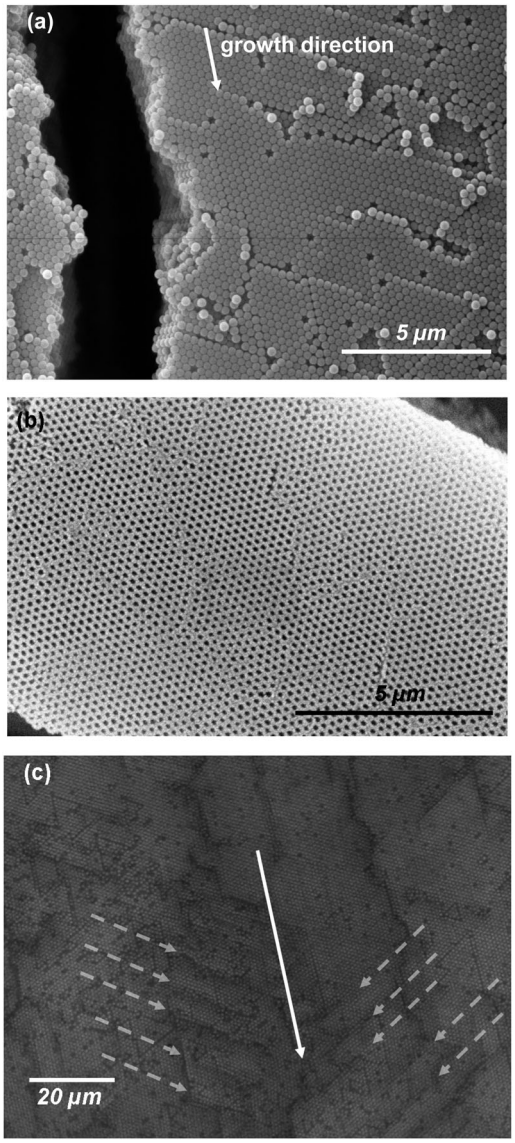

Fig. 3 SEM images of (a) opal and (b) inverse opal films. (c) Fishbone-like pattern of linear defects on the opal film surface. The image was taken by a confocal microscope. The opal film in the last image consists of spheres with a diameter of 920 nm.

Mostly they form an angle of 60° with the growth direction **g**. This feature can also be observed on some VD-made samples.[15] Furthermore, 60° angles of the surface lines with respect to each other and even equal-sided triangles[5] can sometimes be observed. These special arrangements are also visible in some other pictures in the literature.[9,16,17] However, their frequency of occurrence might be overestimated since these arrangements are very attractive and might, therefore, more often be considered as representative.

Nevertheless, the line-like surface defects are always appearing. They have been assigned to edge dislocations[5] or, in more works, to stacking faults (SFs) which form an angle of 70.5° with respect to the substrate.[9,10,18] SFs are typical disturbances of close-packed systems.[14,19] They have been analyzed more in detail for VD-made opals emphasizing the possibility of different kinds of SFs. Recent investigations[9] of VD-made samples by X-ray diffraction have been interpreted with so-called double stacking faults. In addition, coherent X-ray diffractive imaging has been applied to reconstruct interesting parts of the real lattice of a VD-made sample. It shows a clear example of such a double stacking fault.[10] The investigated area in both mentioned works is however very small (7 μm for the diffraction) and one typically focuses in such works on an interesting part like a SF or on one single structural domain only. Therefore, the question of the frequency of occurrence of these parts remains an issue. In our neutron scattering experiments, the illuminated area is much larger and the results will represent statistical averages.

In comparison with the PS spheres of the opal films, the hollow spheres of inverse opals are visibly smaller. The sizes of the hollow spheres seem to be of similar homogeneity like those of the PS spheres. The crystal pieces separated by cracks have much smaller dimensions than their opal mold (typically 10 μm in comparison with 100 μm for the opals). On the scale shown in Fig. 3(b), the lattice is of good quality. The alignment of the lattice fluctuates slightly more than in opal films (about ±2° in comparison with about ±1°). One should however note that the fabrication procedure for the inverse opals, especially the temperature treatment, has an influence on the inverse opal lattice parameters[20] and also on the sample quality. The applied procedure is a result of a fabrication optimization and delivers good and reproducible samples. In our investigations, other procedures always resulted in a lower sample quality, concerning homogeneity, crystalline ordering, and crack distance.

Summarizing the above mentioned observations, inverse opals contain more crystal disturbances than its opal mold while the inversion preserves the crystalline structure in general.

3.2 Position and shape of the peaks in the SANS pattern

The diffraction pattern of the opal and inverse opal films at normal incidence ($\omega = 0$) shows six nearly symmetric bright spots, some features at lower angles, and a relatively strong background (Fig. 4). The latter is considerably higher for inverse opals. The brightest spots are 220-type reflections. This assignment can be concluded from the SEM pictures (hexagonally ordered surface) and from the known systematic extinctions of the fcc lattice. The spot positions are in accordance with the positions calculated from Bragg's law for 220-type reflections. The specific assignment (see Fig. 4(f)) can be made by using two different assumptions on the orientation of the fcc lattice.[13] Therefore, there are two different possibilities for the specific labeling.

The exact positions of the peaks have been determined by their center of mass (CM) which is the intensity-weighted average of the k-vectors in the spot area: $\mathbf{Q}_{CM} = \Sigma_i \mathbf{Q}_i I(\mathbf{Q}_i)/\Sigma_i I(\mathbf{Q}_i)$. Practically, this determination was carried out by an iterative algorithm to exclude the influence of the choice of a finite spot area.

To check the symmetry of the diffraction patterns, all peaks except peak 1 were rotated by multiples of 60° around the center into the segment of peak 1 (indicated in Fig. 4(c)). As visible in Fig. 4(b) and (e), the peaks show slight deviations

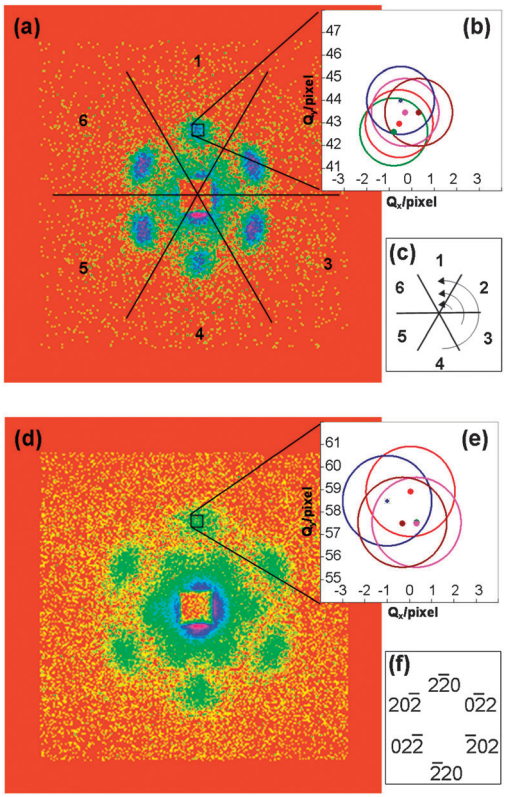

Fig. 4 (a) Neutron diffraction pattern of an opal film. (b) The position of peak n (bright spots) after rotation by $(n - 1) \times 60^\circ$ around the center. The errors of these positions are shown by circles around each point (n = 1: blue, 2: green, 3: red, 4: gray, 5: pink, 6: brown). (c) Scheme of the rotation process. (d) Diffraction pattern for an inverse opal film. (e) The same position analysis as in Fig. 4(b) but for the inverse opal. (f) Peak assignment according to one of the two fcc lattices. The low-angle region of the data in Fig. 4(a) and (d) has already been analyzed in ref. 14. For better visibility, the two patterns have different color codes and illumination times.

from hexagonally symmetric positions. However, these deviations are inside of the accuracy of the method which is shown by the circle around each spot position. The magnitude of this accuracy was estimated by the maximum deviation of Friedel-related peaks from each other (1.5 or 2 pixels for direct or inverse opals, respectively).

A visible deviation from hexagonal symmetry seems to be the different shape of the peaks. The two peaks on the vertical axis have circular shape while the others appear elliptical. However, after rotating the sample around the Z_S axis by 90° the circular peaks transform to the elliptical form. Therefore, these shape variations have to be attributed to the properties of the primary neutron beam. The influence of sample quality on the spot shape is difficult to discuss because of this effect of the neutron beam properties.

The lattice constant difference between the opal and the corresponding inverse opal can be well determined from these measurements. The peaks are distributed on a circle with the radius of 43.5 pixels for the opal and 58 pixels for the inverse opal. This means a shrinkage to (75 ± 2)% during the inversion process.

In order to investigate the lattice structure also in out-of-surface directions, the sample was rotated around the Y_L axis.

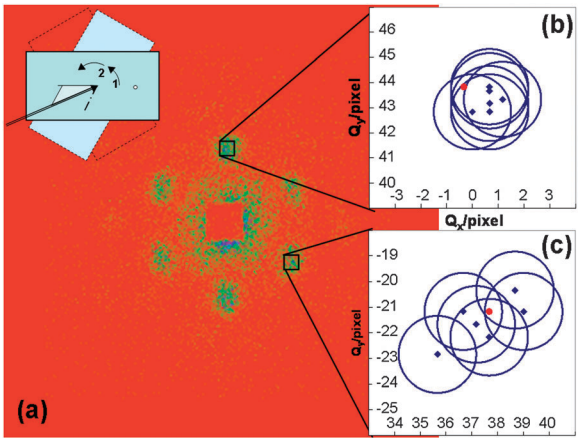

Fig. 5 (a) Scheme of the χ-rotation experiment probing the different {111} directions and the cumulated diffraction pattern for the six different orientations. The individual patterns from the directions $[11\bar{1}]_{fcc1}$, $[1\bar{1}1]_{fcc2}$, $[\bar{1}11]_{fcc1}$, $[11\bar{1}]_{fcc2}$, $[1\bar{1}1]_{fcc1}$, and $[\bar{1}11]_{fcc2}$ do not show visible differences. (b) and (c) Peak positions of the individual patterns. The red dots are the peak positions observed in the [111] direction.

At ω = 68°, the neutron beam is almost parallel to the $[11\bar{1}]$ direction. Furthermore, keeping ω = 68° fixed, the sample was rotated in 60° steps around the Z_S axis (χ-rotation) to probe the other directions of the ⟨111⟩ family. All the six measurements show very similar hexagonal diffraction patterns. This is surprising because only 3 directions belong to this family. Therefore, the result is not consistent with a single fcc lattice only, but with a twinned structure as published in ref. 13. Three patterns originate from one twin and the other three from the other. The peak positions of all the 68° measurements turn out to be the same as at the normal incidence for all six different measurements (Fig. 5).

On the one hand there seems to be no sign for a lattice deformation in the neutron diffraction data, but on the other hand there are clearly anisotropic influences on the lattice during fabrication. The interaction with the support must be directed into the [111] direction. Growth and drying processes proceed in the $[1\bar{1}0]$ direction. The drying process induces the known[4] anisotropic crack pattern. The anisotropic superstructure of linear surface defects described in the last section must be generated by a combination of deposition and support influences. However, despite these anisotropic influences, the fcc lattice parameters are not anisotropically disturbed. There is no flow-induced deformation as well as no support-induced deformation. Quantitatively, this statement is restricted to a measurement accuracy of 1.5 pixels in the diffraction pattern (opal). This corresponds to 12.5 nm in the real space. From this value, it can be concluded that, if there is any deviation from the perfect fcc lattice, it must be below 3.3% in length or below 2° in angle.

The lattice constant calculated from the diffraction pattern is 361 nm for the opal film prepared with 264 nm polystyrene spheres. This value corresponds to a center-to-center distance of 255 nm which is 3% smaller than polystyrene sphere diameter. The difference is slightly larger than the accuracy of our measurement. Because 6 peaks are used for the lattice constant determination the accuracy is a little better than

that of the individual peak positions ($3.3\%/\sqrt{6} = 1.3\%$). Therefore, we can conclude a slight deformation of spheres which we ascribe to physical sintering of the spheres during opal formation as in a former work.[12] In the case of inverse opal films, the lattice diameter is 269 nm which corresponds to the average diameter of the hollow spheres of about 190 nm. This is 28% smaller than the PS sphere size. These data are in well agreement with the former determination of the shrinkage by SEM.[20] The value is also in the range of the already reported values of shrinkage for the inverse opals made by the sol–gel method.[21]

3.3 Forbidden peaks

In addition to the 220-type peaks, there are also less intensive peaks with smaller diffraction angles at hexagonally symmetric positions. At these positions diffraction peaks are forbidden for the fcc lattice. Their intensity is lower, but still of comparable order of magnitude than the allowed peaks.

The existence of these peaks was reported also in other works,[7,9] but assigned to non-fcc lattices. We have shown in a former work that surface effects can explain their appearance.[14] According to this work, the ratio of surface signals to volume signals increases with the width of the peaks in reciprocal space. Since this width is relatively high for colloidal crystals surface signals can reach a high intensity (up to 20% of the volume-allowed peaks). The appearance of similar quasi-forbidden peaks has also been found in different soft matter systems such as liquid crystalline phases.[22]

3.4 Intensity differences of symmetry-related peaks

Apart from the fact that the 220-type diffraction peaks are on hexagonally symmetric positions, the opal peaks show clearly different intensities which violates the fcc symmetry. At normal incidence, the peaks on the Q_y axis (“on-axis peaks”) show significantly less intensity than the peaks with $Q_x \neq 0$ (Fig. 4(a)). In the 68° measurements, this asymmetry is reversed, but less pronounced.

Fig. 6 shows the intensity of the different 220-type peaks for opal and inverse opals quantitatively. The (**Q**/−**Q**)-correlated peaks have almost similar intensity. This correlation is required by Friedel’s law leading to the equal intensity of the hkl and $\bar{h}\bar{k}\bar{l}$ reflections in reciprocal space.[23] The small deviation

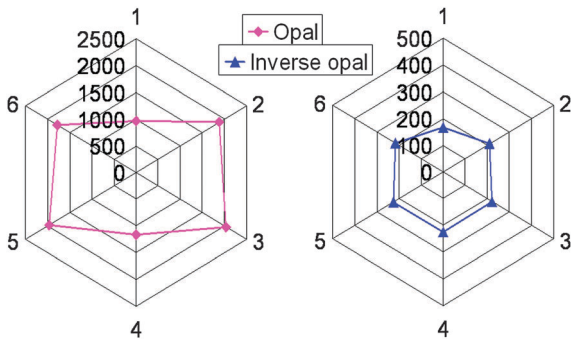

Fig. 6 Background-subtracted intensity of the different diffraction peaks (in counts, simplified polar plot). To allow direct comparison, the effect of longer illumination time was corrected for the inverse opal count numbers.

from the symmetry for the correlated peaks is attributed to a slight misalignment of the sample in connection with the curvature of the Ewald sphere.

For the interpretation of the lower intensity of the on-axis peaks, we propose to consider the influence of a non-symmetric distribution of plane-like lattice perturbations such as SFs. SFs have already been discussed for colloidal crystals and similar systems in general[17] and also in respect to the broadening of Bragg spots.[19]

SFs separate the crystal into domains. These domains generate the same diffraction pattern, but with different phases of the scattered waves. Because of the superposition of these waves, the domain boundaries have a significant influence on the intensity of the spots. If the domain boundaries are non-symmetrically distributed, as discussed in Section 3.1, a non-symmetric diffraction pattern can result. Taking into account the different number of SFs in the different crystal directions one finds (see Appendix):

$$I_{220} = |F_0|^2\alpha$$
$$I_{20\bar{2}} = |F_0|^2\tfrac{2}{2}(1 + \alpha) \qquad (1)$$

with the non-symmetry parameter $\alpha = (1 + n_1)/(1 + n_2)$ containing n_1 for the number of SFs oriented parallel to the growth direction and n_2 for the number of SFs oriented in one of the other directions (appearing as fishbone lines in Fig. 3). The intensity measurements shown in Fig. 6 lead to $\alpha = 0.34$ for our opals. This means that we have about 3 times more domains separated by SFs with “fishbone orientation” than domains separated by SFs parallel to the growth direction.

The intensity differences between spots are much less visible in the case of the inverse opal. The non-symmetry parameter changes to $\alpha = 0.81$. This almost disappearance of non-symmetry effects very likely results from the interplay of oriented SFs with other domain boundaries (called statistical boundaries in the appendix). These domain boundaries become more important because of the high number of the additional cracks and deformations in the inverse opal.

3.5 Rocking curves

Rocking curves can be used to analyze domain orientations. Fig. 7 shows them for the opal films. They display narrow peaks around $\omega = 0$ for the off-axis peaks and nearly a constant behavior for on-axis peaks. This difference is expected since the reciprocal lattice points generating the on-axis peaks stay inside the Ewald sphere during rotation whereas the off-axis peaks cross it.

The curves for all off-axis peaks are very similar; therefore, they have been added together as shown in Fig. 7(a). There are pronounced peaks at about 0° and at the largest measured angles. As far as visible they are of similar shape. At 70° the neutron beam is theoretically in the [11$\bar{1}$] direction explaining the reappearance of the 220-type peaks. The small increase around $\omega = 36°$ in Fig. 7(a) is likely the contribution of a part of 113-family peaks in the measurement area.

The two on-axis peaks slightly increase with incident angle. The peaks show a small difference in intensity which we ascribe to a small misalignment of the sample. The angular dependence of the peaks should be connected with the changing

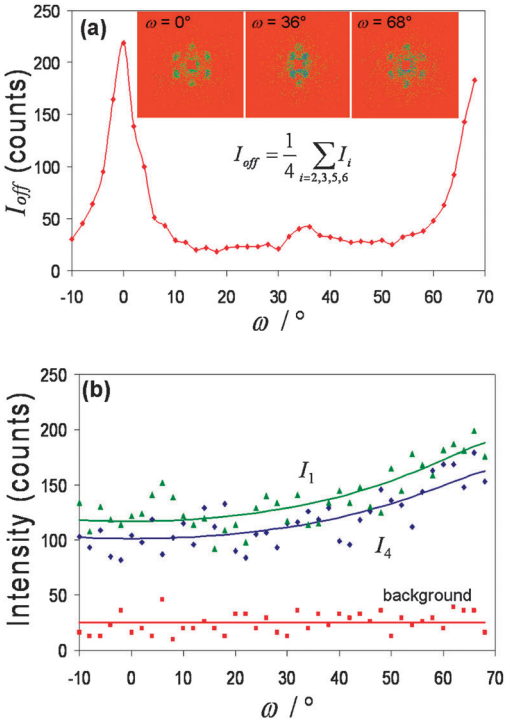

Fig. 7 Intensity profile of the (a) off-axis and (b) on-axis peaks. The solid lines in (b) are fits described by $I = (A_i/\cos\omega)e^{-0.3/\cos\omega}$ with $A_1 = 101$ and $A_4 = 117$. The subscripts are the peak indices as introduced in Fig. 4(a).

effective sample thickness with incident angle. Thicker samples scatter the neutrons stronger into the measured spots but they also attenuate (scatter coherently or incoherently) the neutron beam more. We remember that hydrogen-containing samples have been investigated in the case of the opals. The increase of scattering by sample thickness leads to a $\cos^{-1}$ factor. The increased neutron extinction generates an exponential damping factor. Taken together they lead to the functional behavior as noted in the caption of Fig. 7.

To study the shape of the rocking curves in more detail, Fig. 8 shows them for an opal and in comparison with the correlated inverse opal. There is a clearly visible difference in the two curve widths. The FWHM is 6.2° and 22°, respectively. Obviously, the chemical inversion process for fabricating the inverse opal is a source of lattice misalignments.[24] The shrinkage of the lattice during inversion induces additional cracks and also other visible deformations. This also affects the alignment of the scattering domains relative to each other. However, these large fluctuations are not visible in SEM pictures (see Section 3.1). There, the observed regions are much smaller than the ones tested in neutron scattering. Therefore, also long-range disturbances like the additional cracks formed during inversion have a significant effect on the result.

The measured data do not allow a statement on the curve shape for the inverse opals, however, in the case of the opals the rocking curve data can be better fitted to a Lorentzian curve than to a Gaussian curve. This is an indication for the direct influence of stacking faults on the curve shape.[19] Misalignment of the lattice alone would lead to Gaussian rocking curves. Therefore, we conclude that the misalignment

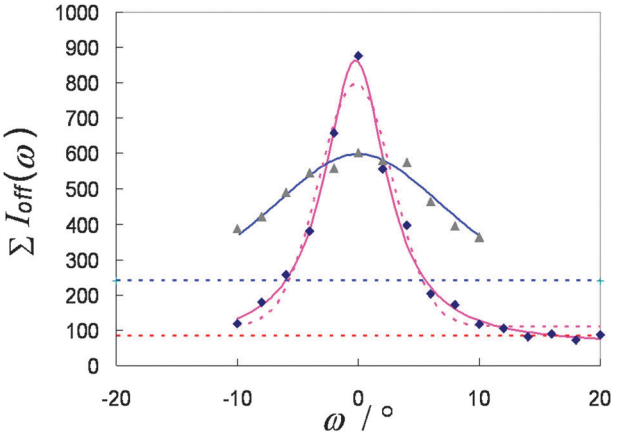

Fig. 8 Rocking curves of an opal film (◆) and an inverse opal film (▲) fitted by Lorentzian and Gaussian (dashed line) profiles. The symbols represent the total intensity of the four off-axis 202-type peaks. Horizontal dotted lines show the average background of opal (lower) and inverse opal (upper), respectively. The effect of the different illumination times was not corrected.

of the lattice can only be a part of all broadening origins and that it must be smaller than the value indicated by the FWHM.

Nevertheless, the long-range lattice deformations described by a mosaic model[19,23] are a very probable interpretation for a large part of the rocking curve width. Based on this model one can conclude that the parts of the opal lattice are aligned better than ±3°, whereas the fluctuation of inverse opal alignment is about ±11°. Since this analysis was made with a neutron beam with a diameter of 4 mm, these values can be regarded as characteristic for the whole film.

4 Conclusions

The SANS investigations on CDM-made opal films have shown an almost perfect fcc structure without any systematic non-symmetric deformations. Opal deposition as well as the opal shrinkage during drying does not seem to generate such deformations although these processes are clearly anisotropic.

However, a growth-related asymmetry was found in the scattering intensities. We associated them to non-randomly distributed plane-like lattice perturbations such as stacking faults.

A Lorentzian shape of the rocking curves has been observed. It is likely that this shape can be assigned to the existence of stacking faults as well.

Based on the rocking curve widths, the alignment fluctuations of the mosaic parts of the sample films made by the CDM are smaller than ±3° for the opals and about ±11° for the inverse opals. We assume that this enhancement of lattice fluctuations is typical for many sol–gel based procedures of opal inversion.

Appendix: Influence of oriented domain boundaries on the diffraction intensities

Plane-like perturbations of a lattice divide the lattice volume into domains. Therefore, these perturbations are also called boundaries. The domains are generally related by

$$\mathbf{r}_I = \mathbf{A}_I\mathbf{r}_0 + \mathbf{S}_I \qquad \text{(A1)}$$

This equation also characterizes the boundary between the domains. The transformation matrix **A** and the shift vector **S** can be statistical or they can have distinct values related with the lattice. In the first case we will call the boundary statistical, in the second case lattice-related (LR). This induces a hierarchy of the domains: different domains separated by LR boundaries form a superdomain together.

The most prominent statistical boundaries in opals are cracks, but also micro-cracks (lattice disruptions below the lattice constant), deformation boundaries, and most growth boundaries belong to that. The mostly regarded LR boundaries are stacking faults (SFs). They are likely most frequent, even though also other types of boundaries[5] may play a role. LR boundaries are characterized by orientation parameters and phase (length of the shift vector). The orientation described by the direction of the shift vector will turn out as most important for the following calculation.

As discussed in the main text, the distribution of LR boundaries has very likely not the full cubic symmetry (called there "non-symmetric"). There are many LR boundaries with non-zero inclination angles with **g**, but only a few including the **g**-direction. In the following we will concentrate our discussion on SFs as an example for LR boundaries. Since there are 4 different possible SF orientations compatible with the fcc lattice and 2 of them contain **g** in the SF plane, we have only two possible orientations left. We indicate the superdomains containing either one or the other type of SFs with A and A', A for the type of superdomains highlighted with color in Fig. A1 and A' for the other superdomain type where all the SFs are tilted differently.

For calculation of the scattering intensities one has to average over the different superdomains. Since superdomains are interrelated by statistical shift vectors their phase relations average out. However, within a superdomain the different domains contribute to the scattering amplitude with crucially important phase relations. This difference in handling is described by:

$$I = \langle |F|^2 \rangle = \frac{M}{2}\left[\left\langle \left|\sum_{n=1}^{N} F_n^A\right|^2 \right\rangle + \left\langle \left|\sum_{n'=1}^{N} F_{n'}^{A'}\right|^2 \right\rangle\right] \qquad \text{(A2)}$$

Here, N is the number of domains separated by SFs within one superdomain and M is the number of superdomains in the beam. The scattering amplitude of every domain is about the same, only different by certain phase factors determined by the scattering vector $\mathbf{G} = \mathbf{k}_{out} - \mathbf{k}_{in}$ multiplied by the lattice shift:

$$F_n = F_0 \exp(-i\mathbf{G}\mathbf{S}_n) \qquad \text{(A3)}$$

With this approximation we find for large N:

$$\begin{aligned}\sum_{n=1}^{N} F_n^A &= F_0 \sum_{n=1}^{N} \mathrm{e}^{-i\mathbf{G}\mathbf{S}_n} \\ &\approx F_0 \begin{cases} N & \text{if } \mathbf{G}\mathbf{S}_n = 0, 2\pi, \ldots \forall n \\ \sqrt{N}\mathrm{e}^{i\varphi} & \text{otherwise} \end{cases}\end{aligned} \qquad \text{(A4)}$$

φ is a statistical phase factor. For the second part of eqn (A4) it was used that the sum of the exponential phase factors forms a special random walk in the complex plane if not all phase factors of the value 1. The specialty of the random walk is the equal step width of 1 and only three allowed directions. Nevertheless, the Einstein random walk formula is valid and the average length of the walk (sum of phase factors) is $\sqrt{N}$. The restriction to the three directions is not important for the result and requires a closer examination of all possible SFs (not in the scope of this paper). It shows that there are only 3 possible values of the vector product $\mathbf{G}\mathbf{S}_n$.

The main peaks in the diffraction pattern can be assigned to different 220-type reflections as shown in Fig. 4 which are connected with different vectors **G**. Sometimes these vectors **G** are perpendicular to the lattice shift $\mathbf{S}_n$. This case refers to the first line of eqn (A4) or, in physical terms, to a perfect constructive interference. In most cases, however, the interference is partially destructive described by the second case in eqn (A4). We summarize the result for three reflections:

$$\begin{aligned}\begin{pmatrix} I_{2\bar{2}0} \\ I_{20\bar{2}} \\ I_{02\bar{2}} \end{pmatrix} &= \frac{MN^2}{2}\left[\begin{pmatrix} \frac{1}{N} \\ \frac{1}{N} \\ 1 \end{pmatrix} + \begin{pmatrix} \frac{1}{N} \\ 1 \\ \frac{1}{N} \end{pmatrix}\right] \\ &= c_0|F_0|^2 \begin{pmatrix} \alpha \\ \frac{1+\alpha}{2} \\ \frac{1+\alpha}{2} \end{pmatrix} \text{ with } \alpha = 1/N\end{aligned} \qquad \text{(A5)}$$

and $c_0 = MN^2$. The other 3 reflections have the same intensity because of Friedel's law.

The assumption of perfect disappearance of SFs along the growth direction can be released and the calculation can straightforwardly be generalized to an arbitrary distribution of SFs characterized by the domain numbers N_1 and N_2. Then, the last result (A5) is the same, only the parameter α has to be replaced by $\alpha = N_1/N_2$. For small $N_{1/2}$ the calculation has to be modified; it is however assumed that the final result would have a very similar structure. The domain numbers used here is connected to the number of SFs in one superdomain $n_{1/2}$ by $N_{1/2} = 1 - n_{1/2}$.

As already noted, stacking faults are likely the most frequent LR boundary type. However, the above theoretical consideration is not restricted to them. A more detailed discussion of the effects of stacking faults and other boundaries requires, however, deeper investigations and are out of the scope of this paper.

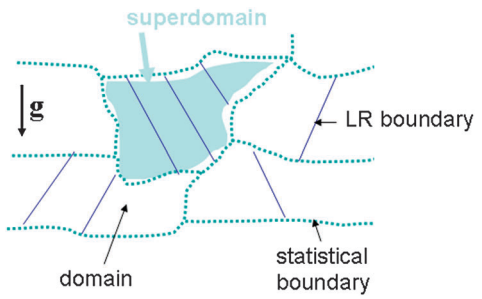

Fig. A1 Scheme for the distinction of different boundaries as well as domain types.

Acknowledgements

We acknowledge H. Zabel and C. Lehmann for very valuable discussions and V. Dyatkin for his kind and important help during the neutron scattering experiments. S. Palm is acknowledged for the SEM images and T.-S. Deng for the confocal microscopy images. The IMPRS for Surface and Interface Engineering in Advanced Materials (SurMat) and German Research Foundation (SFB 558) are thanked for their support.

References

1 E. Yablonovitch, *Phys. Rev. Lett.*, 1987, **58**, 2059–2062.
2 S. John, *Phys. Rev. Lett.*, 1987, **58**, 2486–2489.
3 P. Jiang, J. F. Bertone, K. S. Hwang and V. L. Colvin, *Chem. Mater.*, 1999, **11**, 2132–2140.
4 H.-L. Li, W. Dong, H. J. Bongard and F. Marlow, *J. Phys. Chem. B*, 2005, **109**, 9939–9945.
5 F. Marlow, Muldarisnur, P. Sharifi, R. Brinkmann and C. Mendive, *Angew. Chem., Int. Ed.*, 2009, **48**, 6212–6233.
6 J. H. J. Thijssen, A. V. Petukhov, D. C. 't Hart, A. Imhof, C. H. M. van der Werf, R. E. I. Schropp and A. van Blaaderen, *Adv. Mater.*, 2006, **18**, 1662–1666.
7 A. Sinitskii, V. Abramova, N. Grigorieva, S. Grigoriev, A. Snigirev, D. V. Byelov and A. V. Petukhov, *Europhys. Lett.*, 2010, **89**, 14002.
8 A. A. Eliseev, D. F. Gorozhankin, K. S. Napolskii, A. V. Petukhov, N. A. Sapoletova, A. V. Vasiliev, N. A. Grigoryeva, A. A. Mistonov, D. V. Byelov, W. G. Bouwman, K. O. Kvashnina, D. Y. Chernyshov, A. A. Bosak and S. V. Grigoriev, *JETP Lett.*, 2009, **90**, 272–277.
9 J. Hilhorst, V. V. Abramova, A. Sinitskii, N. A. Sapoletova, K. S. Napolskii, A. A. Eliseev, D. V. Byelov, N. A. Grigoryeva, A. V. Vasilieva, W. G. Bouwman, K. Kvashnina, A. Snigirev, S. V. Grigoriev and A. V. Petukhov, *Langmuir*, 2009, **25**, 10408–10412.
10 J. Gulden, O. M. Yefanov, A. P. Mancuso, V. V. Abramova, J. Hilhorst, D. Byelov, I. Snigireva, A. Snigirev, A. V. Petukhov and I. A. Vartanyants, *Phys. Rev. B: Condens. Matter Mater. Phys.*, 2010, **81**, 2241051–2241056.
11 H. Graetsch and K. Ibel, *Phys. Chem. Miner.*, 1997, **24**, 102–108.
12 I. Popa and F. Marlow, *ChemPhysChem*, 2008, **9**, 1541–1547.
13 M. Muldarisnur and F. Marlow, *J. Phys. Chem. C*, 2011, **115**, 414–418.
14 F. Marlow, M. Muldarisnur, P. Sharifi and H. Zabel, *Phys. Rev. B: Condens Matter Mater. Phys.*, 2011, **84**, 073401.
15 K. Wostyn, Y. Zhao, B. Yee, K. Clays, A. Persoons, G. de Schaetzen and L. Hellemans, *J. Chem. Phys.*, 2003, **118**, 10752–10757.
16 B. Lange, F. Fleischhaker and R. Zentel, *Phys. Status Solidi A*, 2007, **204**, 3618–3622.
17 J.-M. Meijer, V. W. A. de Villeneuve and A. V. Petukhov, *Langmuir*, 2007, **23**, 3554–3560.
18 Y. A. Vlasov, V. N. Astratov, A. V. Baryshev, A. A. Kaplyanskii, O. Z. Karimov and M. F. Limonov, *Phys. Rev. E*, 2000, **61**, 5784–5793.
19 A. Guinier, *X-ray Diffraction in Crystals, Imperfect Crystals and Amorphous Bodies*, W.H. Freeman & Co., San Francisco, 1963.
20 W. Dong and F. Marlow, *Microporous Mesoporous Mater.*, 2007, **99**, 236–243.
21 A. Stein, F. Li and N. R. Denny, *Chem. Mater.*, 2008, **20**, 649–666.
22 S. Foerster, A. Timmann, C. Schellbach, A. Frömsdorf, A. Kornowski, H. Weller, S. V. Roth and P. Lindner, *Nat. Mater.*, 2007, **6**, 888–893.
23 C. Giacovazzo, *Fundamentals of Crystallography*, Oxford University Press, New York, 1998.
24 J. E. G. J. Wijnhoven, L. Bechger and W. L. Vos, *Chem. Mater.*, 2001, **13**, 4486–4499.